

Cite this: *Energy Environ. Sci.*,  
2025, 18, 10460

# Unveiling the role of halide mixing in the crystallization kinetics and charge transfer mechanisms of wide-bandgap organic–inorganic halide perovskites

Nian Li,<sup>†,ab</sup> Shambhavi Pratap,<sup>†,bc</sup> Renjun Guo,<sup>id \*d</sup> Zirui He,<sup>id e</sup> Suzhe Liang,<sup>b</sup> Xiangkun Jia,<sup>f</sup> Mohammad Gholipour,<sup>d</sup> Finn Babbe,<sup>id g</sup> Nicola S. Barchi,<sup>g</sup> Jonathan L. Slack,<sup>c</sup> Nobumichi Tamura,<sup>c</sup> Liang Qiao,<sup>id \*a</sup> Carolin M. Sutter-Fella,<sup>id \*gh</sup> and Peter Müller-Buschbaum,<sup>id \*b</sup>

Despite many efforts to increase the photovoltaic performances of wide-bandgap (WBG, with a Br content above 20%) perovskite solar cells based on bromine–iodine (Br–I) mixed-halide perovskites, understanding the crystallization kinetics of WBG perovskite films, as well as the role of Br mixing in the crystallization kinetics, is still lacking. Furthermore, an overlooked aspect is the correlation of the halide compositions, crystallization kinetics, crystallographic structure, and charge transfer dynamics. Here, we unveil that Br–I mixed-halide WBG perovskite films undergo two intrinsically different crystallization kinetic processes. One is the intermediate solvent-complex phase-assisted growth (I-rich), and the other is top-to-bottom downward growth (Br-rich). Such downward growth (including high Br concentrations) correlates with the formation of a highly vertically oriented perovskite film, which is accompanied by defect formation caused by a dissolving and recrystallization process coupled with halide homogenization. Consequently, Br-rich WBG perovskite films exhibit enhanced charge carrier transport, but are concurrently plagued by non-radiative charge recombination. Addressing this fundamental perspective is critical to precisely tailor Br-related crystallization, which significantly affects the structure and optoelectronic properties of WBG perovskite films and devices.

Received 19th September 2025,  
Accepted 30th October 2025

DOI: 10.1039/d5ee05540g

rsc.li/ees

## Broader context

Understanding the crystallization kinetics of Br–I mixed-halide WBG perovskite films, and their correlation with the crystallographic structure and charge transfer dynamics, is critical for advancing WBG perovskite devices. Herein, this study explores the composition–crystallization–structure–property relationships of WBG mixed-halide perovskite films. Such downward growth (of Br-rich films) correlates with the formation of a highly vertically oriented perovskite film, which is accompanied by defect formation caused by a dissolving and recrystallization process coupled with halide homogenization. Consequently, these films exhibit enhanced charge carrier transport, but are concurrently plagued by non-radiative charge recombination. To maximize the WBG potential, balancing orientation and suppressing non-recombination centers are essential.

<sup>a</sup> School of Physics, University of Electronic Science and Technology of China, Chengdu, 610106, China. E-mail: liang.qiao@uestc.edu.cn<sup>b</sup> Technical University of Munich, TUM School of Natural Sciences, Chair for Functional Materials, James-Frank-Str. 1, 85748, Garching, Germany. E-mail: muellerb@ph.tum.de<sup>c</sup> Advanced Light Source, Lawrence Berkeley National Laboratory, Berkeley, USA<sup>d</sup> Institute of Microstructure Technology (IMT), Karlsruhe Institute of Technology (KIT), Hermann-von-Helmholtz-Platz 1, 76344, Eggenstein-Leopoldshafen, Germany. E-mail: renjun.guo@kit.edu<sup>e</sup> CNOOC Gas & Power Group Co. Ltd, Beijing, 100028, China<sup>f</sup> Laboratory of Zhongyuan Light, School of Physics, Zhengzhou University, 100 Kexue Avenue, Zhengzhou, 450001, China<sup>g</sup> Chemical Sciences Division, Lawrence Berkeley National Laboratory, Berkeley, USA. E-mail: csutterfella@lbl.gov<sup>h</sup> Molecular Foundry, Lawrence Berkeley National Laboratory, Berkeley, USA<sup>†</sup> These authors contributed equally to this work.

## Introduction

Perovskite-based tandem solar cells have demonstrated rapid and impressive breakthroughs in power conversion efficiencies (PCEs). Wide-bandgap (WBG) perovskites, as the top subcell, can be integrated with many emerging photovoltaic technologies, such as silicon (Si), copper indium gallium selenide (CIGS), low bandgap perovskites, or organic solar cells.<sup>1</sup> The certified PCEs of perovskite/Si and all-perovskite tandem solar cells have reached 33.9% and 29.1%, respectively, exceeding that of single perovskite solar cells (26.1%).<sup>2,3</sup> For state-of-the-art perovskite tandem devices, WBG perovskites commonly utilize iodide–bromide (I–Br) mixed halides with a range of high Br contents (>20%).<sup>4,5</sup> However, perovskite solar cells (PSCs) with mixed halides, especially with a Br content above 20%, suffer from processes leading to non-radiative recombination and phase segregation under operational conditions, which pose major limitations on the performance of WBG perovskite solar cells.<sup>6–9</sup> These issues are linked to the film formation processes within high Br compositions, which undergo rapid and inhomogeneous growth phenomena, resulting in perovskite films with high extents of defects associated with their microstructural features, such as high density of grain boundaries<sup>8,10,11</sup> and compositional heterogeneity.<sup>12</sup>

Addressing the above challenge has seen various strategies from the research community toward the goal of improving Br-rich perovskite film characteristics. These include methods such as compositional texture engineering,<sup>8</sup> interface engineering,<sup>10,13,14</sup> and additive engineering.<sup>15–17</sup> The results from the studies point toward the necessity of understanding how Br modification in perovskite materials affects their crystallization kinetics, exploring the formation processes of various metastable and stable phases, following their temporal and thermodynamic stabilities, and correlating their structural and functional optoelectronic properties.

To date, the crystallization kinetics of organic–inorganic perovskite films with normal band gaps or narrow band gaps have been widely studied by *in situ* grazing-incidence wide-angle X-ray scattering (GIWAXS).<sup>18</sup> However, only a handful of studies have probed the formation dynamics of WBG mixed-halide perovskite films *via in situ* photoluminescence (PL).<sup>7,19,20</sup> For example, An *et al.*<sup>20</sup> and Wang *et al.*<sup>7</sup> investigated the formation kinetics of Br-rich perovskites (60% Br). Huang *et al.* reported that Br<sup>−</sup> affects the formation dynamics and defect physics of WBG perovskite films. Specifically, a Br-rich phase nucleates first, and then reaches the target stoichiometry during the growth stage through a halide homogenization process governed by Br–I interdiffusion, accompanied by the formation of numerous defects.<sup>19</sup> These pioneering studies have provided insights into the role of Br mixing in WBG perovskite formation, and particularly its effects on the defect and optoelectronic properties.<sup>7,19,20</sup> However, a systematic and detailed investigation into the crystallization kinetics of Br-rich (>20% Br) WBG perovskite films and the impacts of anions on their crystallization kinetics, especially orientation transitions, remains lacking. Notably, the crystallization kinetics correlated

with film microstructures, which primarily refer to crystallographic orientation, and charge transfer mechanisms, are yet to be unambiguously established.

The synchrotron-based *in situ* GIWAXS method has proven to be a powerful tool to elucidate the structure evolution processes.<sup>21–24</sup> Moreover, GIWAXS can be combined with complementary *in situ* techniques, such as *in situ* absorption or PL measurements, due to the characteristically strong optoelectronic response of the perovskite materials themselves, thereby enabling multimodal *in situ* characterization studies.<sup>23,24</sup> Beyond multiprobe and correlative characterization studies, developing new instruments enables the correlation of intricate experimental processing accompanied by controllable environments to the crystallization kinetics of perovskite films.<sup>25,26</sup> Therefore, synchrotron-based multimodal *in situ* platforms effectively reveal the underlying mechanisms and enhance the common understanding of WBG perovskite crystallization.

In this work, through systematic GIWAXS and PL multimodal *in situ* experiments, we explore the role of Br<sup>−</sup>/I<sup>−</sup> halogen anions in the crystallization kinetics of Br-rich WBG perovskites. To get a view as fundamental as possible and draw sound conclusions, we mainly focus on an I–Br mixed-halide WBG perovskite system MAPbI<sub>3–x</sub>Br<sub>x</sub> ( $x = 0, 1, 1.5, 2, \text{ and } 3$ ), since it is one of the most classical and widely studied compositions, and simultaneously, the effects of cation inclusion on the perovskite crystallization kinetics can be ruled out. As the Br concentration increases, we observe and analyze two types of crystallization kinetics of one-step solution fabricated WBG perovskite films with antisolvent-drop and thermal-annealing processes: one is an intermediate solvent-complex phase-assisted growth, and another is a top-to-bottom downward growth. Among them, the top-down mode enables the crust of perovskite films to behave as a structural template and induce subsequent growth to form vertically oriented crystallites.<sup>27</sup> During thermal annealing, the dissolving and recrystallization process, accompanied by halide intermixing, leads to the formation of spatially distributed domains of compositional variances within the thin film. Moreover, we develop a detailed understanding of the composition–crystallization–structure–property relationships of WBG mixed-halide perovskite films, ultimately achieving a complete correlation from the atomic/molecular scale to macroscopic device performance. Combining the crystallographic structure and charge transfer processes, we find that perovskite films with a highly vertical orientation will facilitate charge carrier transport. In contrast, the increased defects within the oriented perovskite films lead to non-radiative charge recombination. Notably, the preferred orientation still substantially affects the charge transfer mechanisms within the devices. We propose a unifying perspective towards understanding the phenomena experienced during the *in situ* crystallization of hybrid compositions of perovskite films and further correlate the optoelectronic properties of devices pertaining to the composition with the incipient crystallographic structures established during thin film formation.



## Results and discussion

### Structural and charge carrier dynamics within thin films

In the present work, we investigate I-Br mixed-halide WBG perovskite films, specifically focusing on compositions with a high Br content ranging from 33% to 67%. Although the Br-rich compositions studied exceed the ideal bandgap range typically required for WBG perovskites in tandem solar cells, we aim to systematically explore perovskites with a wide bandgap range, which includes ideal bandgap ranges for tandem solar cells. The ultraviolet (UV)-visible absorption data, X-ray diffraction (XRD) patterns, and morphology information of the  $\text{MAPbI}_{3-x}\text{Br}_x$  films are provided (Fig. S1–S3 and Table S1). These data agree with the reported literature,<sup>28</sup> which confirms an accurate material synthesis.

The crystallographic structure, especially the crystallographic orientation of  $\text{MAPbI}_{3-x}\text{Br}_x$  films, is a critical feature that will influence the optoelectronic properties of WBG perovskite films.

A high degree of preferential vertical orientation is beneficial for charge-carrier extraction and transfer within functional stacking.<sup>29,30</sup> To understand the crystallographic orientation and the order degree of lattice stacking, we perform 2D GIWAXS measurements of  $\text{MAPbI}_{3-x}\text{Br}_x$  films (Fig. 1A). The Debye-Scherrer diffraction ring patterns for the  $\text{MAPbI}_{3-x}\text{Br}_x$  films ( $x = 0, 1$ ) suggest a random orientation of the crystallites.<sup>31</sup> In contrast, a concentrated scattering signal at the out-of-plane direction of the (100) plane for the  $\text{MAPbI}_{3-x}\text{Br}_x$  films ( $x = 1.5$ ) indicates a preferential vertical orientation. Sharp and discrete scattering Bragg spots for the  $\text{MAPbI}_{3-x}\text{Br}_x$  films ( $x = 2, 3$ ) indicate a high degree of vertical orientation. Therefore, we conclude that when the Br concentration increases, an isotropic orientation of the polycrystalline film gradually transfers into a highly out-of-plane preferential orientation, enhancing the desired vertical orientation within films (Fig. S4 and S5).

To gain an insight into the optoelectronic properties of the films, we investigate the spectroscopy characterization studies



**Fig. 1** Structure and charge transfer mechanisms of Br-rich WBG perovskite films. (A) 2D GIWAXS data of  $\text{MAPbI}_{3-x}\text{Br}_x$  films. (B) Photoluminescence lifetime mapping images of the  $\text{MAPbI}_{3-x}\text{Br}_x$  film. Time-resolved PL spectra of (C) bare  $\text{MAPbI}_{3-x}\text{Br}_x$ , (D) PTAA/ $\text{MAPbI}_{3-x}\text{Br}_x$ , and (E)  $\text{MAPbI}_{3-x}\text{Br}_x/\text{PCBM}$  films on glass. (F) Schema depicting the extent of efficient charge transport with different extents of preferential orientation of crystallites within thin films. Strong vertical orientation provides directed channels for efficient charge extraction. Random orientations lead to a directional anisotropy of charge carrier diffusion pathways, which decelerates charge extraction.



of the  $\text{MAPbI}_{3-x}\text{Br}_x$  films. Comparative analysis of PL lifetime mappings (Fig. 1B) reveals a noticeable decrease in photoluminescence lifetime with an increase in Br concentration. To further confirm this tendency, we conducted time-resolved PL (TRPL) measurements of the perovskite films. Fig. 1C shows TRPL decays of the WBG perovskite films, fitted with a mono-exponential decay model<sup>32</sup> (Fig. S6). The fit results reveal that the charge carrier lifetime decreases as the Br content increases, which agrees well with PL lifetime mapping. These results underscore that high-Br concentration perovskite compositions exhibit serious bulk non-radiative recombination processes, which are an indicator of defect states within the perovskite material.<sup>19,20</sup> Additionally, the film morphologies (Fig. S3a–j), examined with scanning electron microscopy (SEM) and atomic force microscopy (AFM), and the evaluation of the size distribution (Fig. S3k–m) show that as the Br content increases, the grain size generally decreases.<sup>8,33</sup> This finding is consistent with the reported literature that a high Br content, causing more rapid crystallization, creates a high density of grain boundaries, which may lead to more defects accompanied by defect-induced charge carrier recombination.<sup>8,34</sup> Therefore, we reason that Br-rich perovskite films (>20% Br) tend to grow with smaller grain sizes and have more defect states in comparison with I-rich ones.

To understand the correlation between the crystallographic orientation and optoelectronic properties of the  $\text{MAPbI}_{3-x}\text{Br}_x$  films, we examine the TRPL data of the  $\text{MAPbI}_{3-x}\text{Br}_x/\text{PTAA}$  and  $\text{MAPbI}_{3-x}\text{Br}_x/\text{PCBM}$  functional stacking layers. The TRPL curves of perovskite/transport layer heterojunctions exhibit bi-exponential decay: a fast initial decay correlates with charge extraction to the transport layer, and the second decay with interfacial recombination.<sup>32</sup> Notably, a rather similar decay trend in the  $\text{MAPbI}_{3-x}\text{Br}_x$  samples with either PTAA or PCBM implies that as the Br concentration increases, both the charge extraction and the non-radiative recombination losses are enhanced (Fig. 1D and E and Fig. S7, Table S2). This trend is supported by computing the differential lifetime (Fig. S8), proposed by Yuan *et al.*<sup>35</sup> Unlike full device architectures,<sup>36</sup> our study focuses on the material stack level, where we observe that both PCBM and PTAA, as organic materials, exhibit characteristics that allow us to infer charge transfer dynamics in the presence of a perovskite layer. We assume that boosted charge extraction could be attributed to the vertical crystallographic orientation of the Br-rich perovskite films compared to randomly orientated I-rich perovskites. As pointed out previously,<sup>37</sup> vertical charge carrier diffusivities are primarily affected by the intergrain and intragrain pathways. Moreover, the predominant mode of vertical charge diffusion is the intragrain pathway due to the film thickness, which is generally maintained within the average size range of perovskite crystallite sizes (Fig. S9). In other words, most charge transports are efficiently transported through the direct intragrain pathways.<sup>37</sup> Following this reasoning (as sketched in Fig. 1F), strong vertical orientation within the perovskite films provides direct vertical pathways for electron and hole diffusion,<sup>30</sup> which contributes to fast charge transport. Random orientations within the intragrain

enable the heterogeneity and anisotropy of charge carrier diffusion,<sup>37</sup> which hinders any charge extraction afterward.

### Crystallization kinetics of $\text{MAPbI}_{3-x}\text{Br}_x$ perovskite systems

To figure out the origin of the crystallographic orientation and defect formation of mixed-halide WBG perovskite films, we investigate the crystallization kinetics of  $\text{MAPbI}_{3-x}\text{Br}_x$  perovskite systems *via* synchrotron-based multimodal *in situ* GIWAXS and PL measurements. To achieve this, we use a specially designed instrument, which provides an insight into the thin film crystallization process within a nitrogen environment *via* an antisolvent-assisted spin-coating procedure followed by thermal annealing (Fig. 2A–C).<sup>23,24,38</sup> This protocol has been demonstrated as a general approach for attaining thin films resulting in high-efficiency PSCs.<sup>39</sup>

2D GIWAXS data in Fig. 2D show the key structure conversion before, during, and after the antisolvent drop event. We find that the structural evolution of  $\text{MAPbI}_3$  and  $\text{MAPbI}_2\text{Br}$  films proceeds *via* a similar pathway (Fig. S10), in which both transform from the precursor phase to the cubic perovskite phase through a crystalline intermediate solvent-complex phase (type I). In contrast,  $\text{MAPbBr}_3$  and  $\text{MAPbIBr}_2$  films undergo a direct transformation from the precursor to the cubic perovskite phase, accompanied by pronounced preferential orientations (type II). The crystallization process of the  $\text{MAPbI}_{1.5}\text{Br}_{1.5}$  film incorporates features of both types, thus representing an intermediate case between type I and type II. Notably, we focus on the WBG compositions, with 33%–67% Br. Thus, we regard  $\text{MAPbI}_2\text{Br}$  and  $\text{MAPbIBr}_2$  as the representatives, and further analyze their crystallization kinetics in detail.

**Crystallization kinetics of  $\text{MAPbI}_2\text{Br}$  perovskite films.** Fig. 3A and D (and Fig. S11a) display a simultaneous overview of the temporal evolution of structural and phases of the  $\text{MAPbI}_2\text{Br}$  film, as extracted from *in situ* GIWAXS and PL during perovskite crystallization. To develop an understanding of the evolution of the various emerging chemical phases, we analyze the perovskite (100) and solvent-complex (150) peaks, with regard to peak intensities, positions, and the FWHM values (Fig. 3B and C, and Fig. S11b–d). To trace the phase evolution, the maximum-intensity peak of the individual PL profiles is also analyzed, and thus its peak intensity, position, and FWHM are extracted (Fig. 3E and F, and Fig. S11e). The detailed data treatments are described in SI and Fig. S4. Based on the comprehensive information, we classify the crystallization process into five stages.

In the first stage (Stage I,  $t = 0\text{--}4$  s), the characteristics of diffuse halo signals (Fig. 2D and Fig. S12, S13a) and the lack of PL emission in Stage I (Fig. 3D–F and Fig. S13b) are consistent with the findings reported in the previous literature.<sup>23</sup> With the antisolvent drop at  $t = 5$  s, the diffuse halos shift to the positions at 0.52, 1.62, and 3.04  $\text{\AA}^{-1}$  (Fig. S13e), suggesting a rapid structure change within the precursor phase. Instantly, the signals further transform into low but distinct Bragg diffraction rings at 1.01, 1.44, 1.74, 2.02, 2.26, 2.47, 2.86, and 3.03  $\text{\AA}^{-1}$ , corresponding to  $\text{MAPbI}_2\text{Br}$  (100), (110), (111), (200), (210), (211), (220) and (300) reflections ( $t = 6\text{--}7$  s; Fig. 2D and



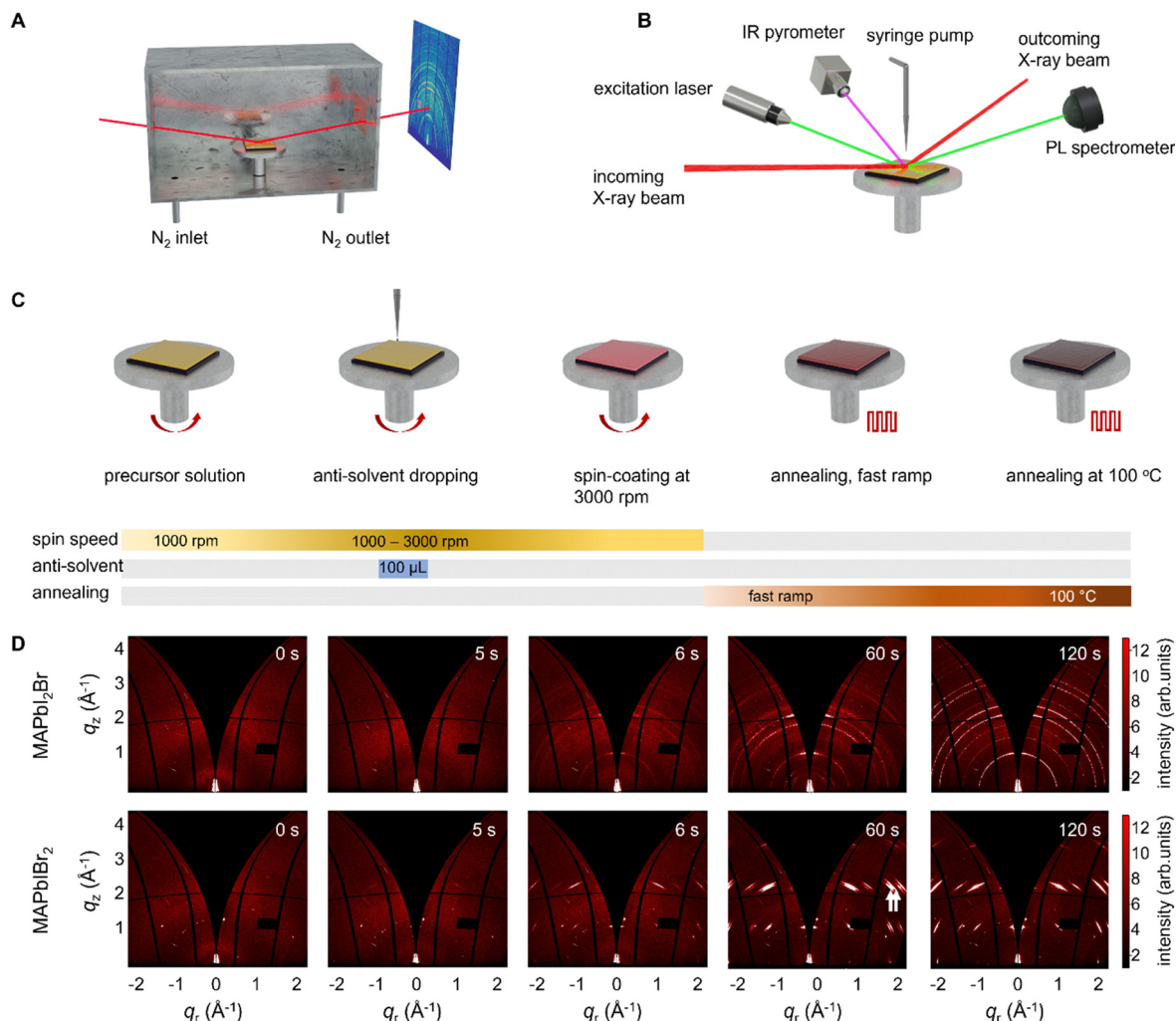


Fig. 2 Sketch of a multimodal *in situ* analytical cell and structural conversion seen in 2D GIWAXS data. (A) and (B) Sketch of a multimodal *in situ* analytical cell highlighting the combined 2D GIWAXS and PL measurements. (C) Sketch of the critical steps during the *in situ* spin-coating standardized procedure. (D) 2D GIWAXS data as a function of the scattering vector components  $q_r$  and  $q_z$  during structural conversion of MAPbI<sub>2</sub>Br and MAPbI<sub>2</sub>Br<sub>2</sub> films before, during, and after the antisolvent drop at  $t = 5$  s.

Fig. S13a).<sup>40</sup> Moreover, the antisolvent drop immediately induces a broad but intense PL peak at  $\sim 642$  nm (Fig. 3D–F and Fig. S13b), which demonstrates a much higher initial energy bandgap ( $\sim 1.93$  eV), compared to the final bulk film ( $\sim 1.77$  eV; Fig. 3F).

In the second stage (Stage II,  $t = 5$ –23 s), besides the cubic perovskite peaks, we can also observe that strong diffraction intensities are present at  $\sim 0.47$ ,  $0.51$ ,  $0.65$ , and  $1.77 \text{ \AA}^{-1}$  (Fig. S12 and S13a and c), which correspond to the orthogonal crystalline solvent-complex, MA<sub>2</sub>Pb<sub>3</sub>(I/Br)<sub>8</sub>·2DMSO (denoted as MAPbI<sub>2</sub>Br·DMSO, details in Fig. S13f).<sup>23</sup> The  $q$  position of the perovskite (100) peak,  $q_{(100)}$ , slightly increases with a narrowing FWHM (Fig. 3C). Correspondingly, the PL peak intensity shows an increase and then a decreasing tendency (Fig. 3E); the PL position varies at  $\sim 650$  nm (1.90 eV; Fig. 3F and Fig. S13b and d). Therefore, we speculate that these observations might be explained by the interplay between crystal growth and crystal dissolution. The small-sized nuclei have a tendency to attach to

the surface of large ones or dissolve, owing to their surface/interfacial energies and high solubilities.<sup>41,42</sup> Via small-cluster coalescence (LaMer mechanism), the size of initial nanocrystals, expected to be above the critical radius and thermodynamically stable, increases and becomes homogeneous. Meanwhile, the small nanocrystals would disappear.<sup>43</sup>

In the third stage (Stage III,  $t = 24$ –64 s), at the end of the spin-coating protocol ( $t = 24$  s), a thermal annealing process of the thin film is initiated. We observe the significant redshifts of PL (the maximum wavelength arriving at  $t = 48$  s) and the narrowing of the peak width (Fig. 3F), and the perovskite  $q_{(100)}$  position overall showing an increasing trend (Fig. 3C). This is attributed to solvent molecules evaporating from the film as the temperature rises. Simultaneously, the Ostwald ripening (also called grain coarsening) could occur during this process.<sup>12</sup> However, the coexistence of perovskite and intermediate phases within the film, with the possible introduction of micro-strain, could contribute to the broadening of the diffraction peak



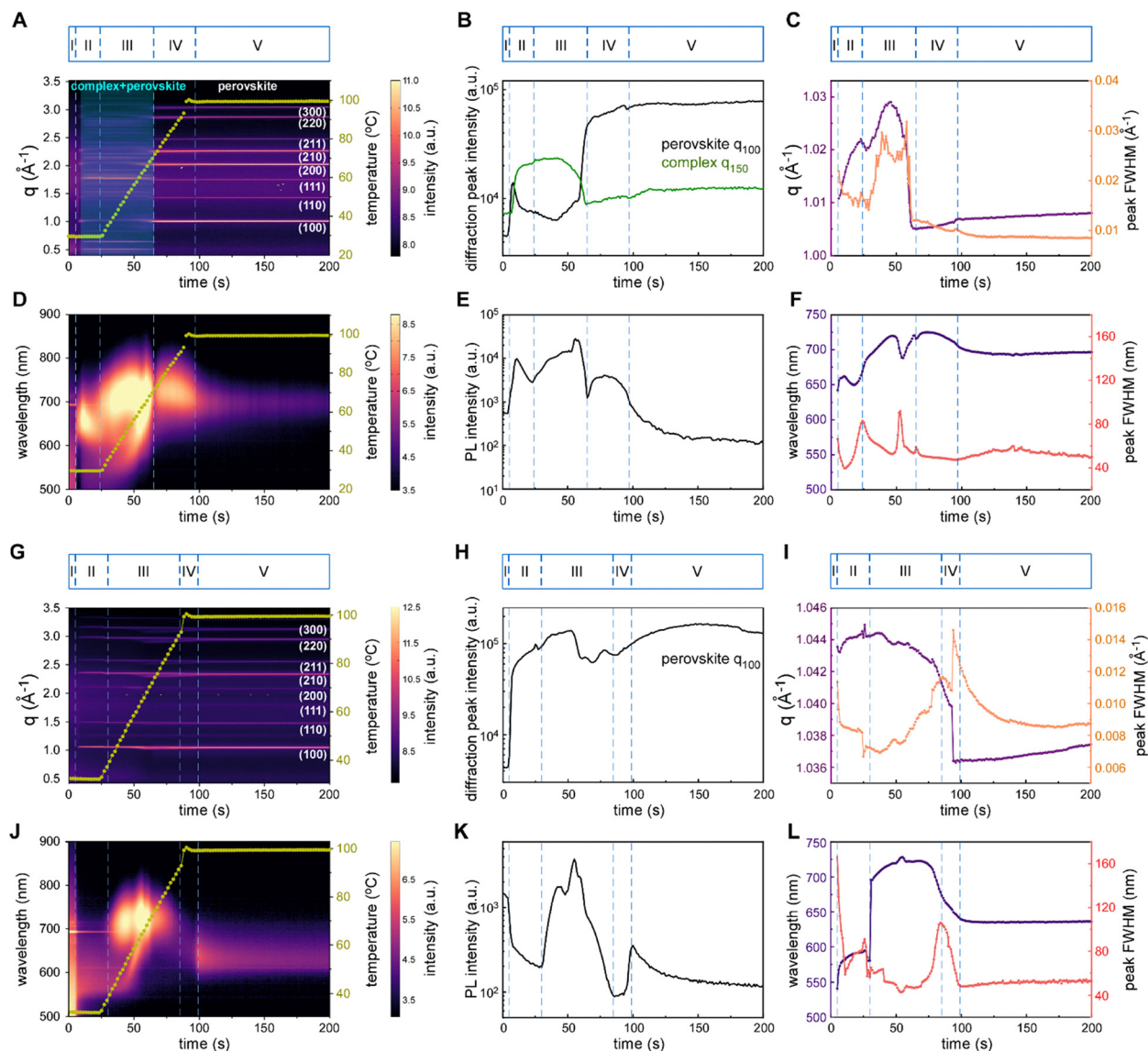


**Fig. 3** Mapping with five stages seen in GIWAXS and PL data, and temporal evolution of characteristic parameters for (A)–(F) MAPbI<sub>2</sub>Br and (G)–(L) MAPbBr<sub>2</sub> films. (A) and (G) Radially integrated 2D GIWAXS data as a function of  $q$  position and (D) and (J) PL data as a function of wavelength together with the substrate temperature (olive). The blue-shaded region in (A) highlights the temporal evolution of the intermediate phases, namely the MAPbI<sub>2</sub>Br-DMSO solvent-complex and cubic perovskite phases. To resolve peak-splitting features observed in (G) and to ensure consistency between the two diffraction maps (A) and (G), the  $q$  range is displayed up to  $3.5 \text{ \AA}^{-1}$ . Temporal evolution of (B) the radially integrated 2D GIWAXS intensity of MAPbI<sub>2</sub>Br (black) and MAPbI<sub>2</sub>Br-DMSO solvent-complex (green), and (C) the  $q$  position of the MAPbI<sub>2</sub>Br (100) peak and its related peak FWHM. Temporal evolution of (E) PL emission intensity, (F) PL peak position, and related peak FWHM in the MAPbI<sub>2</sub>Br film. Temporal evolution of (H) the radially integrated 2D GIWAXS intensity of the MAPbI<sub>2</sub>Br (100) peak, and (I)  $q$  position of the MAPbI<sub>2</sub>Br (100) peak and its related peak FWHM. Temporal evolution of the (K) PL emission intensity, (L) PL peak position, and related peak FWHM in the MAPbI<sub>2</sub>Br film. The division of different stages for MAPbI<sub>2</sub>Br and MAPbBr<sub>2</sub> is determined from characteristic features observed in their time-resolved PL mappings (D) and (J) and the extracted PL intensity profiles (E) and (K). Considering that heating conditions can be regarded as effectively identical for both films, the differences in phase-transition timing (e.g., Stage III) primarily originate from the nature of each material. Stage III for MAPbI<sub>2</sub>Br occurs within  $t = 24\text{--}64 \text{ s}$  (corresponding to  $\sim 30\text{--}70 \text{ }^\circ\text{C}$ ), whereas Stage III for MAPbBr<sub>2</sub> occurs within  $t = 30\text{--}84 \text{ s}$  (corresponding to  $\sim 36\text{--}90 \text{ }^\circ\text{C}$ ).

(Fig. 3C). At  $t = 49\text{--}64 \text{ s}$ , the diffraction intensities of the MAPbI<sub>2</sub>Br-DMSO complex decrease and finally disappear, and diffraction intensities of the perovskite phase gain an order of magnitude in intensity (Fig. 3B and Fig. S14, S15a and c). Accordingly, the PL signal broadens and blue-shifts ( $t = 49\text{--}53 \text{ s}$ ; Fig. 3F and Fig. S15b and d), and subsequently it quickly undergoes narrowing and red-shifting ( $t = 54\text{--}61 \text{ s}$ ).

Thus, we assume the following points: (1) as solvent molecules continue to evaporate, the thermal dissociation of the solvent complex is initiated, which contributes to a polydispersity of the molecular species. (2) After the removal of DMSO, Ostwald ripening drives the fragments into large grains.<sup>23,44</sup> In the meantime, the aforementioned thermal dissociation and structure rearrangement processes also induce a decrease in



complex  $q_{(150)}$  and perovskite  $q_{(100)}$  peak positions (lattice distances increasing), and relatively broad FWHM values (Fig. 3C and Fig. S11b–d).

In the fourth and fifth stages (Stage IV,  $t = 65$ – $96$  s; Stage V,  $t = 97$ – $200$  s), the intensity of the perovskite (100) peak slightly increases and then almost remains constant (Fig. 3B). The  $q_{(100)}$  position slightly increases towards  $\sim 1.007 \text{ \AA}^{-1}$  accompanied by an FWHM narrowing (Fig. 3C). Thus, we assume that as the residual solvent gradually completely evaporates from the deep zone, a denser lattice packing is formed. Besides, we can also observe a slight PL shift towards  $\sim 700$  nm (1.77 eV; Fig. 3F and Fig. S16). This trend is likely attributed to the formation of residual  $\text{PbX}_2$  at grain boundaries.<sup>45</sup> Besides, we note that defect formation can also contribute to this PL blue shift and emission decrease. At the end of the fifth stage, the finished perovskite film is achieved.

#### Crystallization kinetics of the $\text{MAPbIBr}_2$ perovskite film.

Fig. 3G–L shows the mapping with five stages seen in the GIWAXS and PL data, and the temporal evolution of the respective key parameters for the  $\text{MAPbIBr}_2$  film. With the antisolvent drop at 5 s, the diffraction peak at  $\sim 1.05 \text{ \AA}^{-1}$  immediately appears (Fig. 2D and Fig. S17 and S18a). At  $t = 6$  s, the intensities of the diffraction spots at  $\sim 1.05, 1.48, 2.35, 2.57, 2.97,$  and  $3.15 \text{ \AA}^{-1}$  are remarkably enhanced. The prominent scattering spots probably correspond to the perovskite  $\text{MAPbIBr}_2$  or  $\text{MAPbBr}_3$  (100), (110), (210), (211), (220), and (300) reflexes. The PL position at this moment is located at  $\sim 567$  nm ( $t = 6$  s; Fig. 3L). It indicates that the Br-rich composition quickly nucleates in the framework of a cubic crystal structure, with a high degree of preferential vertical orientation (azimuthal angle  $\chi$  of  $0^\circ$ ; the direction normal to the substrate, Fig. S4). As a general crystallization mechanism reported in the literature,<sup>30,46</sup> the initial nucleation of a vertically oriented crust of Br-rich composition proceeds from the liquid–air interface, thereby leading to a high extent of crystallographic preferred orientation (CPO) within thin films.

In the second stage (Stage II,  $t = 5$ – $29$  s), only a cubic perovskite crystal structure is present (Fig. 3G), and its intensity increases with time (Fig. 3H). The 2D GIWAXS data (Fig. 2D and Fig. S17 and S19) manifest that the growth of vertically oriented 3D-perovskite fosters the development of a highly preferentially oriented polycrystalline perovskite phase, bypassing the intermediate solvent-complex phase. Additionally, the  $q_{(100)}$  position generally keeps rising while its FWHM exhibits a downtrend (Fig. 3I), suggesting the presence of a denser and more ordered lattice stacking as a result of the crystal growth. The PL position gradually shifts towards  $\sim 580$  nm (2.13 eV) and remains stable afterward (Fig. 3L). The redshift ( $t = 5$ – $29$  s) can be mainly attributed to a composition gradient evolution, in which the initial Br-rich segments transform into the I-rich within the film over time.<sup>19</sup>

In the third and fourth stages (Stage III,  $t = 30$ – $84$  s; Stage IV,  $t = 85$ – $98$  s), the thermal annealing process commences from  $\sim 32$  °C ( $t = 25$  s). Herein, a strong PL emission is observed, initially centered at  $\sim 700$  nm (Fig. 3L and Fig. S20a), indicating that the I-rich phase immediately emerges at the top region.

The PL signal undergoes a redshift to  $\sim 728$  nm ( $t = 30$ – $54$  s; Fig. 3L). Meanwhile, the first peak also exhibits a redshift, and eventually merges with the second peak, showing a non-Gaussian peak shape (Fig. 3J). At  $t = 54$  s, the perovskite  $q_{(100)}$  signal gradually splits into two peaks, and then fuses together (Fig. 3G and Fig. S20c and d) at  $t = 93$  s. This phenomenon can also be observed in other diffraction peaks (yellow arrows in Fig. S21a), where the peaks become asymmetric before reverting to a symmetric shape. The emergent PL peak at  $\sim 700$  nm and the split diffraction Bragg peak at  $\sim 1.021 \text{ \AA}^{-1}$  (as denoted by white arrows in Fig. 2D; blue arrows in Fig. S20c and d) both confirm that the initial Br-rich composition at the top layer is quickly replaced by an I-rich composition during the early stages of thermal annealing. We attribute this behavior to a rapid dissolving–recrystallizing process driven by heat and mass transfer, primarily at the air–film interface, where solvent mass transfer is significant in the “fast” drying stage.<sup>47</sup> This stage occurs within one second,<sup>47</sup> and provides the conditions for the previously formed Br-rich upper layer to dissolve. Moreover, the diffusion and exchange processes of the anions are necessary to achieve halide homogenization and finally obtain the stoichiometry from the initially Br-rich-containing species.<sup>19</sup> The ion diffusion is related to the low activation energy for  $\text{I}^-/\text{Br}^-$  migration and ion concentration gradient across the film thickness, which can be further accelerated by heat/solvent transfer.<sup>48</sup> In addition, the mechanism of vacancy- and interstitial-mediated ion diffusion could also be considered.<sup>49,50</sup> Consequently, anions diffuse outward from the crystal and diffuse toward to re-construct the  $\text{PbX}_6$  polyhedrons.<sup>51</sup> Such a dissolution and recrystallization process accompanied by self-diffusion and homogeneity of anions is reflected in the splitting and merging of the PL peaks and  $q_{(100)}$  peaks (Fig. 3G and J, and Fig. S20). Additionally, such a homogeneity process is reported to assist defect formation.<sup>19,52</sup> In the fourth stage ( $t = 85$ – $98$  s), the PL signal shows a distinct blueshift and a wide distribution (Fig. 3L and Fig. S22). In the fifth stage (Stage V,  $t = 99$ – $200$  s), the constant PL position centered at  $\sim 635$  nm (1.95 eV) is representative of luminescence from a stable  $\text{MAPbIBr}_2$  film, and the  $q_{(100)}$  peak position centered at  $\sim 1.037 \text{ \AA}^{-1}$  is consistent with having reached the final perovskite film. Again, at the end of the fifth stage, the final perovskite film results in a highly preferential orientation (Fig. S23).

#### Origin of crystallographic orientation and stacking defects.

Grasping the crystallization kinetics of WBG perovskite films is foundational to governing film quality parameters such as crystallization orientation and defect generation. Although there are several reports on film formation, there remains a need for a comprehensive understanding of critical phase transitions and nucleation/growth mechanisms, particularly the role of Br modification in the crystallization kinetics.

In the first scenario, we propose an intermediate phase-assisted growth<sup>23</sup> process within the I-rich perovskite film, as sketched in Fig. 4A and C. First, the perovskite phase nucleates at the air–liquid interface, forming thin clusters with a relatively random orientation. The continuous solvent evaporation



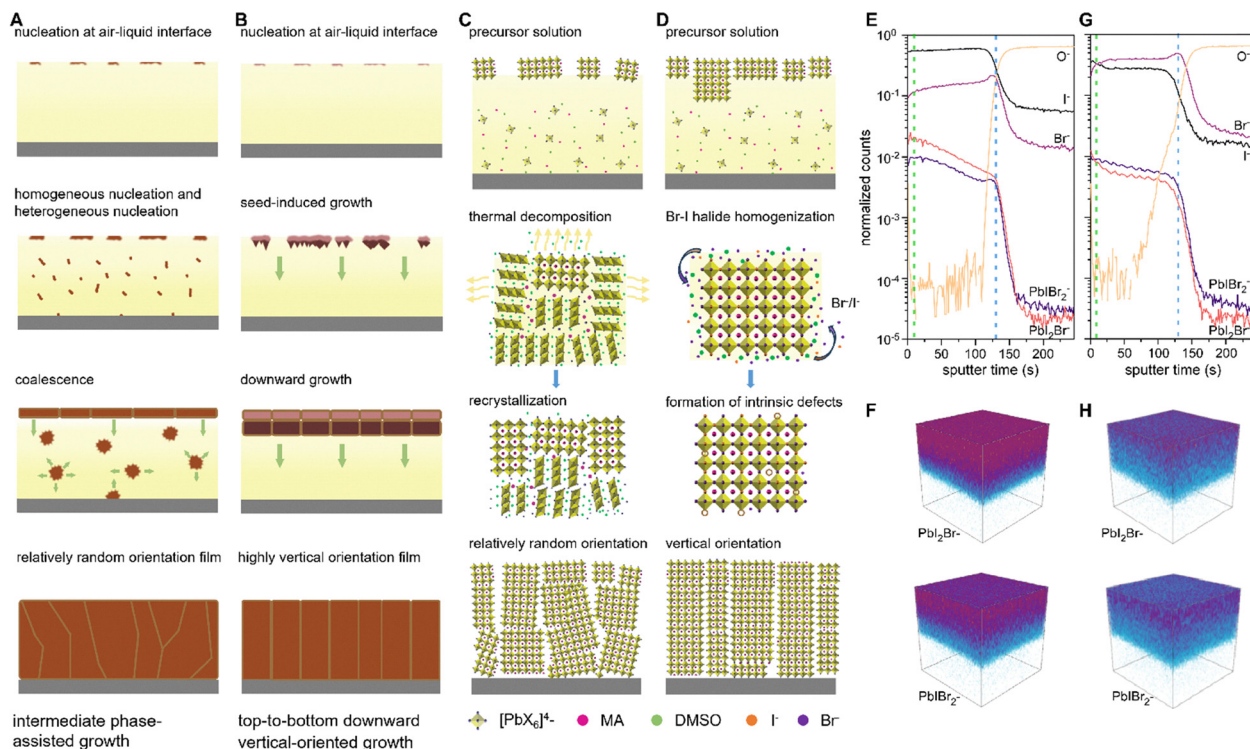


**Fig. 4** Crystallization kinetics and compositions of WBG perovskite films, tailored by the Br content. Schematic illustration of two types of crystallization kinetics processes: one is intermediate phase-assisted growth (A) and (C), and the other is top-to-bottom downward vertical-oriented growth (B) and (D). As the Br concentration increases, the intermediate phase-assisted growth mode (I-rich) transforms into the top-to-bottom downward vertical-oriented growth (Br-rich). Accordingly, a polycrystalline perovskite film with random orientations transforms into a near-single-crystalline-quality perovskite film with highly vertical orientations. ToF-SIMS depth profiles of (E) MAPbI<sub>2</sub>Br and (G) MAPbIBr<sub>2</sub> films deposited on an ITO substrate. The corresponding ion distribution of Pbl<sub>2</sub>Br<sup>-</sup> and PblBr<sub>2</sub><sup>-</sup> in (F) MAPbI<sub>2</sub>Br and (H) MAPbIBr<sub>2</sub> films. The green and blue dashed lines denote the regions of the surface and bulk of the films, respectively.

provides the supersaturation at the air-liquid interface that drives the crystal growth of the initial nuclei. Besides, the supersaturation is also consumed by the nucleation of the intermediate solvent-complex phase, probably in the forms of heterogeneous nucleation at the interfaces and the homogeneous nucleation within the bulk of the solution.<sup>21,27</sup> These nucleation modes could drive growth in all space directions,<sup>53</sup> as indicated by the perovskite phase coexisting with the intermediate phases (Stage II; Fig. S11). Upon thermal annealing, crystal domain evolution and grain growth occur through grain coarsening, accompanied by the thermal decomposition of the solvent-complex into Pb-X fragments and recrystallization into the cubic MAPbI<sub>2</sub>Br crystals with relatively random orientations.<sup>23</sup>

In the latter scenario, we speculate on having a top-to-bottom downward vertical-oriented growth for the Br-rich perovskite films, as illustrated in Fig. 4B and D. Vertically oriented Br-rich perovskites nucleate at the air-liquid surface. This initial high degree of preferential vertical orientation is probably related to the surface energy or surface chemistry.<sup>54</sup> To confirm this, we performed density functional theory (DFT) calculations and calculated the surface energies of the (100) and (110) planes. Aligned with the study on MAPbBr<sub>3</sub>,<sup>55</sup> the (100)-terminated slab of MAPbIBr<sub>2</sub> has a lower surface energy in comparison to other lattice planes (Table S3), and

therefore dominates on the surface (blue box at  $t = 5$  s; Fig. S18a). The Br-rich composition has a faster crystal growth rate, which can effectively consume the increasing solution concentration to suppress additional nucleation.<sup>27</sup> The thin crust acts as a structure template to guide the subsequent growth process (also referred to as seed-induced growth). Furthermore, in this downward mode, the (100) plane with more rapid vertical growth continues to maintain its dominance. The 2D GIWAXS data primarily show a similar pattern after 6 s, agreeing well with this proposed growth mode. Interestingly, the crystal nucleation/growth rate trend (100) > (110) is consistent with the XRD peak intensities of different planes (Fig. S2). During the annealing and drying process, apart from the grain coarsening, the residual solvent removal enables access to the dissolution and re-crystallization of the top surface. Simultaneously, the Br-I anions undergo diffusion and exchange, where they migrate across the whole film. We explain such phenomena with the assistance of heat/solvent transfer and a vertical gradient of Br<sup>-</sup>/I<sup>-</sup> ion distribution,<sup>48</sup> probably accompanied by an interstitial- and vacancy-mediated ion diffusion mechanism.<sup>49,50</sup> Based on the above PL lifetime mapping and TRPL result, we speculate that such a homogeneity process has a higher possibility of causing native point defect-like vacancies, as well as interstitials and anti-site occupations,<sup>56</sup> as compared to the first scenario. We conclude



that the crystallization kinetics, including drying kinetics, which lead to different nucleation and growth modes, are critical for the film structure. In particular, the heterogeneous nucleation and top-to-bottom growth modes, along with the lower surface energy of the (100) crystal plane, may correlate with a highly out-of-plane preferential orientation (vertical orientation). This finding is also applicable to the FAMA-based system, to a certain extent (Fig. S24).

Unlike MAPbI<sub>2</sub>Br, the MAPbIBr<sub>2</sub> perovskite displays no detectable intermediate phase during crystallization. This difference can be attributed to the distinct coordination chemistry of Pb<sup>2+</sup> with halides and DMSO.<sup>57</sup> In Br-rich formulations, the Pb–Br bond is stronger than the Pb–DMSO interaction, whereas in I-rich systems, Pb–I is weaker than Pb–DMSO. Consequently, the I-rich precursor tends to form stable MAPbX<sub>3</sub>–DMSO intermediate complexes that contributes to the strong intermediate-phase diffraction during film formation. In contrast, the Br-rich MAPbIBr<sub>2</sub> precursor undergoes direct crystallization of the cubic perovskite phase due to the weaker Pb–DMSO interaction and rapid de-solvation. Additionally, the difference in thermodynamic stability between these two compositions also needs to be considered.<sup>58</sup>

To elucidate the depth-dependent phase distribution of the surface and internal perovskite layer, we conducted time-of-flight secondary ion mass spectrometry (ToF-SIMS) measurements on the MAPbIBr<sub>2</sub> and MAPbI<sub>2</sub>Br films (Fig. S25). Indeed, the normalized ToF-SIMS depth profiles reveal that the MAPbIBr<sub>2</sub> film shows a more I-rich perovskite phase at the surface (Fig. 4G; black curve), which indicates that the initial Br-rich phase is replaced by an I-rich one. Therefore, it is evident that the self-diffusion and homogenization of the anions occur during the drying process. In contrast, the MAPbI<sub>2</sub>Br film exhibits a relatively uniform distribution of the I<sup>−</sup> ions along the surface normal as seen with the initial sputtering time (Fig. 4E; black curve). The more uniform distribution of I<sup>−</sup> ions in MAPbI<sub>2</sub>Br compared to MAPbIBr<sub>2</sub> is likely due to the formation of an intermediate phase (MAPbI<sub>2</sub>Br–DMSO) during the initial stages of crystallization.<sup>59</sup> The intermediate phase (MAPbI<sub>2</sub>Br–DMSO) can prolong the processing window of the dropping antisolvent.<sup>59</sup> Moreover, DMSO coordinates with the PbX<sub>2</sub> framework, building a scaffold that allows I<sup>−</sup>/Br<sup>−</sup> ions to distribute more evenly. This is consistent with previous studies that have observed that intermediate phases can improve the homogeneity of perovskite films.<sup>59</sup> The ion distribution result (Fig. 4F and H) agrees with the above findings that the MAPbIBr<sub>2</sub> film has spatially distributed domains of compositional variances. In both films, we observe a gradient distribution of PbI<sub>2</sub>Br<sup>−</sup> and PbIBr<sub>2</sub><sup>−</sup> ions (a downward slope in Fig. 4E and G), which likely indicates compositional gradients across the depth. This phenomenon might be related to a vertical gradient of crystallization (or solvent-induced recrystallization process) from the film–air surface to the film–substrate interface.<sup>60</sup> Moreover, the distribution of Br<sup>−</sup> ions is increased at the film–substrate interface for both films (Fig. 4E and G; purple curves), which is consistent with the report that formation energies of Br immediate adduct phases, like PbBr<sub>2</sub>, are

smaller compared to I-containing species,<sup>19</sup> thus giving rise to effective reduction in the total interface energy.

### Charge transfers within the devices

The charge extraction in devices is critical in verifying our assumption, which is that increasing the Br ratio in perovskite materials can enhance the charge extraction processes in perovskite solar cells (PSCs). We fabricate a series of PSCs as the p–i–n architecture (ITO glass/PTAA/perovskite/PCBM/BCP/Ag) based on the studied composition. The champion power conversion efficiencies (PCEs) achieve 20.91%, 16.59%, 14.78%, 11.64% and 7.54% for MAPbI<sub>3</sub>, MAPbI<sub>2</sub>Br, MAPbI<sub>1.5</sub>Br<sub>1.5</sub>, MAPbIBr<sub>2</sub>, and MAPbBr<sub>3</sub>, respectively (Fig. S26). The photovoltaic performances (Table S4) reach the reported record for MAPbI<sub>1–x</sub>Br<sub>x</sub> WBG PSCs.<sup>28,61</sup> To quantify the effect of crystallographic orientation on the charge extraction within the PSC devices, we first performed light intensity-dependent transient photocurrent (TPC) measurements on the solar cells. Fig. 5A–D shows TPC results on the devices under varying light intensities of 100.0% (1 sun), 31.6%, 10.0% and 3.0%, respectively. Accordingly, the extracted photocurrent decay time as a function of the light intensity is shown in Fig. 5E. We find that MAPbI<sub>1.5</sub>Br<sub>1.5</sub>-based devices obtain the shortest decay time, indicating an enhanced charge transport process compared to the other compositions.<sup>62</sup> Furthermore, we carry out the intensity-modulated photocurrent spectroscopy (IMPS) measurements to jointly confirm enhanced charge carrier transport by increasing the Br ratio and quantify transport time in PSCs (Fig. S27).<sup>63</sup> Fig. 5F shows the extracted lifetime at different offset voltages and the calculated average lifetime. In general, the tendency of the average lifetimes (0.35, 0.49, 0.51, 0.56, and 1.19 μs for the MAPbI<sub>2</sub>Br, MAPbI<sub>1.5</sub>Br<sub>1.5</sub>, MAPbBr<sub>3</sub>, MAPbIBr<sub>2</sub>, and MAPbI<sub>3</sub>, respectively) is consistent with the aforementioned TPC results. The extracted charge extraction times within the full devices exhibit a behavior differing from those in functional stacking layers (Fig. 1D and E). This differentiation is attributed to the different characterization techniques and enhanced complexity inherent in the geometrical configurations of the samples.<sup>64</sup> Finally, we propose that the moderate combination of preferred orientation, grain boundary, and intrinsic defects enables improved charge transport within the devices, particularly when the film thickness exceeds the average grain size.

Combining our results from charge transfer mechanisms (Fig. 1C–E) and charge extraction in PSCs (Fig. 5A–F), we find that increasing the Br ratio achieves the desired vertical orientation in the perovskite materials. This improved crystal orientation enhances the charge carrier transport and extraction, leading to a higher theoretical fill factor.<sup>65</sup> However, this crystal orientation modification also introduces stronger non-recombination centers. Therefore, to further enhance the PCE in WBG PSCs, we recommended developing functional additives or introducing a hot-air blowing or gas-quench technique into different deposition methods (which can change not only the film formation process but also the drying process), to suppress the strong material heterogeneity and non-recombination centers rather than only modifying the





**Fig. 5** Charge carrier extraction within the Br-rich WBG perovskite solar cell devices. Normalized transient photocurrent decay curves of  $\text{MAPbI}_{3-x}\text{Br}_x$  ( $x = 0, 1, 1.5, 2$ , and  $3$ ) perovskite solar cells under (A) 100.0%, (B) 31.6%, (C) 10.0% and (D) 3.0% light intensity. (E) Extracted photocurrent decay time for the  $\text{MAPbI}_{3-x}\text{Br}_x$  perovskite solar cells as a function of the light intensity. Here, we define lifetime as the time at which  $1 - 1/e$  ( $\sim 63.0\%$ ) of the total photocurrent has been detected following the signal pulse, hence accounting for the charge extraction rates. (F) Intensity-modulated photocurrent spectroscopy analysis for  $\text{MAPbI}_{3-x}\text{Br}_x$  perovskite solar cells: lifetimes at different offset voltages ( $-1\text{ V}$ ,  $-0.5\text{ V}$ ,  $0\text{ V}$ ,  $0.5\text{ V}$ , and  $1\text{ V}$ ). The charge transfer time constant ( $\tau_{\text{ct}}$ ) is subtracted from the frequency where the imaginary part of the IMPS quantity reaches a maximum. The average charge transfer time (denoted with the dashed line) is the average value under different bias conditions for each composition material.

preferential crystal orientation.<sup>6,66</sup> Through a balance between the crystal orientation modification and the suppression of non-recombination centers in perovskites, this approach will unlock the full potential of WBG perovskite materials to reach their theoretical limits.

## Conclusions

In summary, by using synchrotron-based GIWAXS and PL multimodal characterization studies, we unravel the crystallization kinetics of Br-I mixed-halide WBG perovskite films. Two different types of crystallization kinetic processes occur within the  $\text{MAPbI}_{1-x}\text{Br}_x$  perovskite films: one is intermediate phase-assisted growth, and the other is top-to-bottom downward vertical-oriented growth. As the Br concentration increases, the intermediate phase-assisted growth mode (I-rich composition) transforms into top-to-bottom downward vertical-oriented growth (Br-rich composition). Notably, the thin film surface with a highly vertical orientation serves as a structural template that guides the crystal growth. Correspondingly, a vertically oriented textured polycrystalline perovskite film is formed, which facilitates charge carrier transport and extraction. Simultaneously, the dissolution and recrystallization process, accompanied by halide homogenization that occurs upon thermal annealing, probably promotes defect formation, thereby contributing to non-radiative charge recombination.

The  $\text{MAPbI}_{1.5}\text{Br}_{1.5}$ -based devices obtain the shortest decay time, indicating a balanced result of crystal orientation modification and the suppression of non-recombination centers in perovskites. The findings of this work will help the perovskite community to understand the crystallization kinetics of WBG perovskite films, particularly the effects of halide mixing on crystallization and crystallographic orientation. The heterogeneous nucleation and top-to-bottom growth modes, along with a specific crystal plane with relatively low surface energy, correlate with the oriented perovskites. These insights are also applicable, to some extent, to mixed-cation Br-rich WBG systems, such as  $\text{MA}_y\text{FA}_{1-y}\text{PbI}_{1-x}\text{Br}_x$ . As a result, this work provides useful guidance to tailor the nucleation/growth process of perovskite films and film structures toward high optoelectronic properties.

## Author contributions

Conceptualization: N. L., R. G., and S. P.; methodology: C. M. S. F., N. T., S. P., and J. L. S.; investigation: N. L., R. G., S. P., F. B., N. S. B., T. B. S., J. L. S., N. T., C. M. S. F., Z. H., X. J., and M. G.; writing – original draft: N. L., and R. G.; writing – review & editing: all authors; funding acquisition: P. M. B., C. M. S. F., and L. Q.; resources: P. M. B., C. M. S. F., and L. Q.; administration: P. M. B., C. M. S. F., and L. Q.; and supervision: P. M. B., C. M. S. F., and L. Q.



## Conflicts of interest

There are no conflicts to declare.

## Data availability

The data generated during this study are included in the published article. The additional information, including supplemental methods, XRD, SEM, AFM, TRPL analysis, 2D GIWAXS patterns and related analysis, ToF-SIMS, *J-V*, IMPS and DFT calculation, are included in supplementary information (SI) and source data files. Supplementary information is available. See DOI: <https://doi.org/10.1039/d5ee05540g>.

The raw 2D GIWAXS and PL data can also be found at the following public repository: <https://doi.org/10.14459/2022MP1688636>. Any additional information required for the data reported in this paper is available from the lead contact upon reasonable request.

## Acknowledgements

This work was supported by funding from the Deutsche Forschungsgemeinschaft (DFG, German Research Foundation) under Germany's Excellence Strategy – EXC 2089/1 – 390776260 (e-conversion), TUM.solar in the context of the Bavarian Collaborative Research Project Solar Technologies Go Hybrid (SolTech), the Center for NanoScience (CeNS), and the International Research Training Group 2022 Alberta/Technical University of Munich International Graduate School for Environmentally Responsible Functional Hybrid Materials (ATUMS). N. L. acknowledges support from the National Natural Science Foundation of China (Grant No. 12504085) and Natural Science Foundation of Sichuan Province (Grant No. 2025ZNSFSC0861). S. P. acknowledges support from the TUM International Graduate School of Science and Engineering (IGSSE) via the GreenTech Initiative Interface Science for Photovoltaics (ISPV) of the EuroTech Universities, the Bavaria California Technology Center (BaCaTeC), and the Centre for Nanoscience (CeNS). Special thanks are extended to the Nanosystems Initiative Munich (NIM) and the generous ALS Doctoral Fellowship in Residence for funding and administrative support that made this work possible. The authors appreciate the resources and technical support from the Analysis and Testing Center, University of Electronic Science and Technology of China. This research used resources of the Advanced Light Source, a U. S. DOE Office of Science User Facility under contract no. DE-AC02-05CH11231, beamline 12.3.2. C. M. S.-F. and F. B. acknowledge support from the Laboratory Directed Research and Development (LDRD) Program of Lawrence Berkeley National Laboratory under U. S. Department of Energy Contract DE-AC02-05CH11231.

## References

- G. Yang, Z. Ni, Z. J. Yu, B. W. Larson, Z. Yu, B. Chen, A. Alasfour, X. Xiao, J. M. Luther, Z. C. Holman and J. Huang, *Nat. Photonics*, 2022, **16**, 588–594.
- NREL, Best Research-Cell Efficiencies, <https://www.nrel.gov/pv/cell-efficiency.html> (2025).
- M. A. Green, E. D. Dunlop, M. Yoshita, N. Kopidakis, K. Bothe, G. Siefer and X. Hao, *Prog. Photovoltaics Res. Appl.*, 2024, **32**, 3–13.
- R. Lin, Y. Wang, Q. Lu, B. Tang, J. Li, H. Gao, Y. Gao, H. Li, C. Ding, J. Wen, P. Wu, C. Liu, S. Zhao, K. Xiao, Z. Liu, C. Ma, Y. Deng, L. Li, F. Fan and H. Tan, *Nature*, 2023, **620**, 994–1000.
- T. Li, J. Xu, R. Lin, S. Teale, H. Li, Z. Liu, C. Duan, Q. Zhao, K. Xiao, P. Wu, B. Chen, S. Jiang, S. Xiong, H. Luo, S. Wan, L. Li, Q. Bao, Y. Tian, X. Gao, J. Xie, E. H. Sargent and H. Tan, *Nat. Energy*, 2023, **8**, 610–620.
- S. Liu, Y. Lu, C. Yu, J. Li, R. Luo, R. Guo, H. Liang, X. Jia, X. Guo, Y.-D. Wang, Q. Zhou, X. Wang, S. Yang, M. Sui, P. Müller-Buschbaum and Y. Hou, *Nature*, 2024, **628**, 306–312.
- J. Wang, L. Zeng, D. Zhang, A. Maxwell, H. Chen, K. Datta, A. Caiazzo, W. H. M. Remmerswaal, N. R. M. Schipper, Z. Chen, K. Ho, A. Dasgupta, G. Kusch, R. Ollearo, L. Bellini, S. Hu, Z. Wang, C. Li, S. Teale, L. Grater, B. Chen, M. M. Wienk, R. A. Oliver, H. J. Snaith, R. A. J. Janssen and E. H. Sargent, *Nat. Energy*, 2024, **9**, 70–80.
- Q. Jiang, J. Tong, R. A. Scheidt, X. Wang, A. E. Louks, Y. Xian, R. Tirawat, A. F. Palmstrom, M. P. Hautzinger, S. P. Harvey, S. Johnston, L. T. Schelhas, B. W. Larson, E. L. Warren, M. C. Beard, J. J. Berry, Y. Yan and K. Zhu, *Science*, 2022, **378**, 1295–1300.
- J. Xu, C. C. Boyd, Z. J. Yu, A. F. Palmstrom, D. J. Witter, B. W. Larson, R. M. France, J. Werner, S. P. Harvey, E. J. Wolf, W. Weigand, S. Manzoor, M. F. A. M. van Hest, J. J. Berry, J. M. Luther, Z. C. Holman and M. D. McGehee, *Science*, 2020, **367**, 1097–1104.
- L. Liu, Y. Yang, M. Du, Y. Cao, X. Ren, L. Zhang, H. Wang, S. Zhao, K. Wang and S. (Frank) Liu, *Adv. Energy Mater.*, 2023, **13**, 2202802.
- H. Tan, F. Che, M. Wei, Y. Zhao, M. I. Saidaminov, P. Todorović, D. Broberg, G. Walters, F. Tan, T. Zhuang, B. Sun, Z. Liang, H. Yuan, E. Fron, J. Kim, Z. Yang, O. Voznyy, M. Asta and E. H. Sargent, *Nat. Commun.*, 2018, **9**, 3100.
- N. Li, S. Pratap, V. Körstgens, S. Vema, L. Song, S. Liang, A. Davydok, C. Krywka and P. Müller-Buschbaum, *Nat. Commun.*, 2022, **13**, 6701.
- C. Chen, Z. Song, C. Xiao, R. A. Awni, C. Yao, N. Shrestha, C. Li, S. S. Bista, Y. Zhang, L. Chen, R. J. Ellingson, C. S. Jiang, M. Al-Jassim, G. Fang and Y. Yan, *ACS Energy Lett.*, 2020, **5**, 2560–2568.
- Z. Liu, J. Siekmann, B. Klingebiel, U. Rau and T. Kirchartz, *Adv. Energy Mater.*, 2021, **11**, 2003386.
- D. H. Kim, C. P. Muzzillo, J. Tong, A. F. Palmstrom, B. W. Larson, C. Choi, S. P. Harvey, S. Glynn, J. B. Whitaker, F. Zhang, Z. Li, H. Lu, M. F. A. M. van Hest, J. J. Berry, L. M. Mansfield, Y. Huang, Y. Yan and K. Zhu, *Joule*, 2019, **3**, 1734–1745.
- D. Kim, H. J. Jung, I. J. Park, B. W. Larson, S. P. Dunfield, C. Xiao, J. Kim, J. Tong, P. Boonmongkolras, S. G. Ji,



- F. Zhang, S. R. Pae, M. Kim, S. B. Kang, V. Dravid, J. J. Berry, J. Y. Kim, K. Zhu, D. H. Kim and B. Shin, *Science*, 2020, **368**, 155–160.
- 17 Z. Liu, C. Zhu, H. Luo, W. Kong, X. Luo, J. Wu, C. Ding, Y. Chen, Y. Wang, J. Wen, Y. Gao and H. Tan, *Adv. Energy Mater.*, 2023, **13**, 2203230.
- 18 M. Qin, K. Tse, T.-K. Lau, Y. Li, C.-J. Su, G. Yang, J. Chen, J. Zhu, U.-S. Jeng, G. Li, H. Chen and X. Lu, *Adv. Mater.*, 2019, **31**, 1901284.
- 19 T. Huang, S. Tan, S. Nuryyeva, I. Yavuz, F. Babbe, Y. Zhao, M. Abdelsamie, M. H. Weber, R. Wang, K. N. Houk, C. M. Sutter-Fella and Y. Yang, *Sci. Adv.*, 2021, **7**, eabj1799.
- 20 Y. An, N. Zhang, Z. Zeng, Y. Cai, W. Jiang, F. Qi, L. Ke, F. R. Lin, S.-W. Tsang, T. Shi, A. K.-Y. Jen and H.-L. Yip, *Adv. Mater.*, 2023, **36**, 2306568.
- 21 Y. Xu, M. Wang, Y. Lei, Z. Ci and Z. Jin, *Adv. Energy Mater.*, 2020, **10**, 1–18.
- 22 J. Wang, S. Luo, Y. Lin, Y. Chen, Y. Deng, Z. Li, K. Meng, G. Chen, T. Huang, S. Xiao, H. Huang, C. Zhou, L. Ding, J. He, J. Huang and Y. Yuan, *Nat. Commun.*, 2020, **11**, 1–9.
- 23 S. Pratap, F. Babbe, N. S. Barchi, Z. Yuan, T. Luong, Z. Haber, T. Bin Song, J. L. Slack, C. V. Stan, N. Tamura, C. M. Sutter-Fella and P. Müller-Buschbaum, *Nat. Commun.*, 2021, **12**, 5624.
- 24 C. M. Sutter-Fella, *Adv. Energy Mater.*, 2021, **11**, 1–7.
- 25 N. Wu, T. Yang, Z. Wang, Y. Wu, Y. Wang, C. Ma, H. Li, Y. Du, D. Zhao, S. Wang, P. Liu, W. Huang, X. Ren, S. (Frank) Liu and K. Zhao, *Adv. Mater.*, 2023, **35**, 2304809.
- 26 S. Wang, T. Yang, Y. Yang, Y. Du, W. Huang, L. Cheng, H. Li, P. Wang, Y. Wang, Y. Zhang, C. Ma, P. Liu, G. Zhao, Z. Ding, S. (Frank) Liu and K. Zhao, *Adv. Mater.*, 2023, **35**, 2305314.
- 27 A. Z. Chen, M. Shiu, X. Deng, M. Mahmoud, D. Zhang, B. J. Foley, S. H. Lee, G. Giri and J. J. Choi, *Chem. Mater.*, 2019, **31**, 1336–1343.
- 28 J. H. Noh, S. H. Im, J. H. Heo, T. N. Mandal and S. Il Seok, *Nano Lett.*, 2013, **13**, 1764–1769.
- 29 Y. Choi, D. Koo, G. Jeong, U. Kim, H. Kim, F. Huang and H. Park, *Energy Environ. Sci.*, 2022, **15**, 3369–3378.
- 30 A. Z. Chen, M. Shiu, J. H. Ma, M. R. Alpert, D. Zhang, B. J. Foley, D.-M. Smilgies, S.-H. Lee and J. J. Choi, *Nat. Commun.*, 2018, **9**, 1336.
- 31 J. A. Steele, E. Solano, D. Hardy, D. Dayton, D. Ladd, K. White, P. Chen, J. Hou, H. Huang, R. A. Saha, L. Wang, F. Gao, J. Hofkens, M. B. J. Roeffaers, D. Chernyshov and M. F. Toney, *Adv. Energy Mater.*, 2023, **13**, 2300760.
- 32 M. Stolterfoht, C. M. Wolff, J. A. Márquez, S. Zhang, C. J. Hages, D. Rothhardt, S. Albrecht, P. L. Burn, P. Meredith, T. Unold and D. Neher, *Nat. Energy*, 2018, **3**, 847–854.
- 33 Y. Liu, K. Lang, H. Han, H. Liu, Y. Fu, P. Zou, Y. Lyu, J. Xu and J. Yao, *J. Energy Chem.*, 2024, **97**, 419–428.
- 34 Y. Tong, A. Najar, L. Wang, L. Liu, M. Du, J. Yang, J. Li, K. Wang and S. Liu, *Adv. Sci.*, 2022, **9**, 1–20.
- 35 Y. Yuan, G. Yan, C. Dressen and T. Kirchartz, *Adv. Energy Mater.*, 2025, **15**, 2403279.
- 36 M. Stolterfoht, V. M. Le Corre, M. Feuerstein, P. Caprioglio, L. J. A. Koster and D. Neher, *ACS Energy Lett.*, 2019, **4**, 2887–2892.
- 37 C. Cho, S. Feldmann, K. M. Yeom, Y.-W. Jang, S. Kahmann, J.-Y. Huang, T. C. Yang, M. N. T. Khayyat, Y.-R. Wu, M. Choi, J. H. Noh, S. D. Stranks and N. C. Greenham, *Nat. Mater.*, 2022, **21**, 1388–1395.
- 38 M. Singh, M. Abdelsamie, Q. Li, T. Kodalle, D.-K. Lee, S. Arnold, D. R. Ceratti, J. L. Slack, C. P. Schwartz, C. J. Brabec, S. Tao and C. M. Sutter-Fella, *Chem. Mater.*, 2023, **35**, 7450–7459.
- 39 A. D. Taylor, Q. Sun, K. P. Goetz, Q. An, T. Schramm, Y. Hofstetter, M. Litterst, F. Paulus and Y. Vaynzof, *Nat. Commun.*, 2021, **12**, 1–11.
- 40 G. G. C. A. O. M. A. Reinoso, *J. Mater. Sci.: Mater. Electron.*, 2018, **29**, 4276–4284.
- 41 M. Jung, S.-G. Ji, G. Kim and S. Il Seok, *Chem. Soc. Rev.*, 2019, **48**, 2011–2038.
- 42 Y. Zhou, O. S. Game, S. Pang and N. P. Padture, *J. Phys. Chem. Lett.*, 2015, **6**, 4827–4839.
- 43 S. Xu, H. Zhang, B. Qiao and Y. Wang, *Cryst. Growth Des.*, 2021, **21**, 7306–7325.
- 44 Q. Hu, L. Zhao, J. Wu, K. Gao, D. Luo, Y. Jiang, Z. Zhang, C. Zhu, E. Schaible, A. Hexemer, C. Wang, Y. Liu, W. Zhang, M. Grätzel, F. Liu, T. P. Russell, R. Zhu and Q. Gong, *Nat. Commun.*, 2017, **8**, 15688.
- 45 Y. Gao, H. Raza, Z. Zhang, W. Chen and Z. Liu, *Adv. Funct. Mater.*, 2023, **33**, 2215171.
- 46 L. Kuai, J. Li, Y. Li, Y. Wang, P. Li, Y. Qin, T. Song, Y. Yang, Z. Chen, X. Gao and B. Sun, *ACS Energy Lett.*, 2020, **5**, 8–16.
- 47 B. Guerrier, C. Bouchard, C. Allain and C. Bénard, *AIChE J.*, 1998, **44**, 791–798.
- 48 E. Bi, H. Chen, F. Xie, Y. Wu, W. Chen, Y. Su, A. Islam, M. Grätzel, X. Yang and L. Han, *Nat. Commun.*, 2017, **8**, 15330.
- 49 M. Ghasemi, B. Guo, K. Darabi, T. Wang, K. Wang, C.-W. Huang, B. M. Lefler, L. Taussig, M. Chauhan, G. Baucom, T. Kim, E. D. Gomez, J. M. Atkin, S. Priya and A. Amassian, *Nat. Mater.*, 2023, **22**, 329–337.
- 50 C. Eames, J. M. Frost, P. R. F. Barnes, B. C. O'Regan, A. Walsh and M. S. Islam, *Nat. Commun.*, 2015, **6**, 7497.
- 51 M. Lai, A. Obliger, D. Lu, C. S. Kley, C. G. Bischak, Q. Kong, T. Lei, L. Dou, N. S. Ginsberg, D. T. Limmer and P. Yang, *Proc. Natl. Acad. Sci. U. S. A.*, 2018, **115**, 11929–11934.
- 52 H. Xue, J. M. Vicent-Luna, S. Tao and G. Brocks, *J. Phys. Chem. C*, 2023, **127**, 1189–1197.
- 53 D. Zheng, F. Raffin, P. Volovitch and T. Pauporté, *Nat. Commun.*, 2022, **13**, 6655.
- 54 C. Ma, M.-C. Kang, S.-H. Lee, S. J. Kwon, H.-W. Cha, C.-W. Yang and N.-G. Park, *Joule*, 2022, **6**, 2626–2643.
- 55 J. Hidalgo, Y. An, D. Yehorova, R. Li, J. Breternitz, C. A. R. Perini, A. Hoell, P. P. Boix, S. Schorr, J. S. Kretschmer and J.-P. Correa-Baena, *Chem. Mater.*, 2023, **35**, 4181–4191.
- 56 J. M. Ball and A. Petrozza, *Nat. Energy*, 2016, **1**, 16149.
- 57 K. Wang, M.-C. Tang, H. X. Dang, R. Munir, D. Barrit, M. De Bastiani, E. Aydin, D.-M. Smilgies, S. De Wolf and A. Amassian, *Adv. Mater.*, 2019, **31**, 1808357.



- 58 S. Shahrokhi, M. Dubajic, Z.-Z. Dai, S. Bhattacharyya, R. A. Mole, K. C. Rule, M. Bhadbhade, R. Tian, N. Mussakhanuly, X. Guan, Y. Yin, M. P. Nielsen, L. Hu, C.-H. Lin, S. L. Y. Chang, D. Wang, I. V. Kabakova, G. Conibeer, S. Bremner, X.-G. Li, C. Cazorla and T. Wu, *Small*, 2022, **18**, 2200847.
- 59 W. Xiang, J. Zhang, S. (Frank) Liu, S. Albrecht, A. Hagfeldt and Z. Wang, *Joule*, 2022, **6**, 315–339.
- 60 S. Chen, X. Xiao, B. Chen, L. L. Kelly, J. Zhao, Y. Lin, M. F. Toney and J. Huang, *Sci. Adv.*, 2021, **7**, eabb2412.
- 61 L. K. Ono, E. J. Juarez-Perez and Y. Qi, *ACS Appl. Mater. Interfaces*, 2017, **9**, 30197–30246.
- 62 Q. Jiang, L. Zhang, H. Wang, X. Yang, J. Meng, H. Liu, Z. Yin, J. Wu, X. Zhang and J. You, *Nat. Energy*, 2016, **2**, 16177.
- 63 S. Ravishankar, A. Riquelme, S. K. Sarkar, M. Garcia-Batlle, G. Garcia-Belmonte and J. Bisquert, *J. Phys. Chem. C*, 2019, **123**, 24995–25014.
- 64 L. Krückemeier, B. Krogmeier, Z. Liu, U. Rau and T. Kirchartz, *Adv. Energy Mater.*, 2021, **11**, 2003489.
- 65 N.-G. Park and H. Segawa, *ACS Photonics*, 2018, **5**, 2970–2977.
- 66 H. Chen, C. Liu, J. Xu, A. Maxwell, W. Zhou, Y. Yang, Q. Zhou, A. S. R. Bati, H. Wan, Z. Wang, L. Zeng, J. Wang, P. Serles, Y. Liu, S. Teale, Y. Liu, M. I. Saidaminov, M. Li, N. Rolston, S. Hoogland, T. Filleter, M. G. Kanatzidis, B. Chen, Z. Ning and E. H. Sargent, *Science*, 2024, **384**, 189–193.

